Dichroic Plasmonic Films Based on Anisotropic Au Nanoparticles for Enhanced Sensitivity and Figure of Merit Sensing

William L Watkins, Antonio Assaf, Geoffroy Prévot, Yves Borensztein

Dichroic Plasmonic Films based on Anisotropic Au Nanoparticles for Enhanced Sensitivity and Figure of Merit Sensing

William L. Watkins, Antonio Assaf, Geoffroy Prévot, Yves Borensztein.*

Sorbonne Université, CNRS, Institut des NanoSciences de Paris, INSP, 4 place Jussieu, F-75005, Paris, France

Cite this: *J. Phys. Chem. C* 2021, 125, 21, 11799–11812 ;
Publication Date: June 03, 2021

https://doi.org/10.1021/acs.jpcc.1c03841

ABSTRACT

Localized surface plasmon resonance (LSPR) of metal nanoparticles are widely used to develop plasmonic sensors, which permit to detect minute amounts of molecular compounds. Two methods of measurements are commonly used. The first most common mode, which investigates the shift in wavelength of the LSPR induced by the analyte, requires the use of high-resolution monochromators. The second mode, based on self-reference or perfect absorbing systems, measures the changes of the signal intensity, and requires the use of sophisticated samples elaborated by lithography techniques. In this article, we adapt the very sensitive transmittance anisotropy spectroscopy technique with anisotropic plasmonic gold films, formed of slightly elongated nanoparticles easily elaborated by grazing deposition on microscopy glass slides. These films display two different LSPR, caused by their morphological anisotropy, as a function of the light polarization. Working at a single wavelength, we experimentally demonstrate an ultrahigh sensitivity to bulk refractive index sensing, with a resolution below $\delta n=10^{-4}$. The factor of merit (FoM*), defined for intensity-based plasmonic sensors, reaches the outstanding value of 23 000, which is due to the null optical anisotropy signal initially measured, thus granting an enhanced optical contrast when changing the RI. Furthermore, sensitivity down to four avidin molecules per square micron of the sample is theoretically shown, which offers a promising route towards easily made ultra-sensitive miniaturized plasmonic sensors, compatible with microfluidic systems, without the need for a monochromator.

INTRODUCTION

Localized surface plasmon resonance (LSPR) in metallic NPs (gold, silver, palladium ...) have been widely exploited for various applications[1]. Because of the enhancement of its electromagnetic field around the NP[2], the LSPR depends strongly on the particles' environment in their immediate vicinity, over a distance of the order of magnitude of the NP's size. Such property permitted to develop, over the past decade, plasmonic systems which have shown their effectiveness for the sensing of gas, molecular compounds or biomolecules[3–7]. The adsorption of target molecules at the surface of the NPs indeed modifies the LSPR, generally causing a spectral shift of the resonance. An important issue is the sensitivity of such plasmonic sensors, and a lot of efforts have been made to improve it [8]. Most studies are based on gold NPs, for multiple reasons: ease elaboration and ease handling, as well as their good stability and chemical inertness. Several avenues have been proposed to improve the sensitivity of gold-based plasmonic sensors. One approach relates to elaborating NPs with judiciously chosen shapes, e.g. nanostars, nanocubes [4,9,10], possibly organized in arrays[10], in order to increase the LSPR spectral shift upon molecule adsorption as well as yielding a narrower resonance, leading to higher factors of merits (FOM). Another path, which can be combined with the former, is the use of narrow Fano resonances achieved thanks to the interaction between different resonant structures [9,11,12]. These methods usually require the determination of the LSPR spectral position with high precision, which needs a high-resolution monochromator [10]. In order to avoid the use of such monochromators, intensity-based sensing has been proposed, e.g. by monitoring the intensity of the signal at the peak or at the slope of the resonance [13]. However, such approach must have a very high measurement stability, which is intrinsically difficult to reach. Lastly, self-reference sensors based on double or triple resonances, as well as almost-perfect absorbing systems, have

been recently proposed [14–16]. Most of the previously referenced methods also require lithographic elaboration techniques, with the disadvantage of high fabrication cost and low yield [4,10,12,14–17].

Here, we propose an alternative approach, which does not require the use of a monochromator and is intrinsically self-referencing. We use films formed of anisotropic gold NPs easily elaborated by grazing incidence vacuum deposition on glass slides, which display two LSPR dependent on the polarization's orientation of the incident light (see Scheme 1). The method is based on the monitoring of the film optical dichroism at a fixed wavelength, specifically the variation in the transmission anisotropy (TA), upon the change of the refractive index of the embedding medium or the adsorption of target molecules. This differential method derives from the reflectance anisotropy spectroscopy (RAS), largely used in surface science for investigating very small optical anisotropy of single crystals with anisotropic structures [18–21]. Similar methods have revealed the possibility of investigating the tarnishing of Ag NPs in air [22], the kinetics surface adsorption of H_2 on Au NPs [23], or the bulk absorption of H_2 in Pd NPs [24].

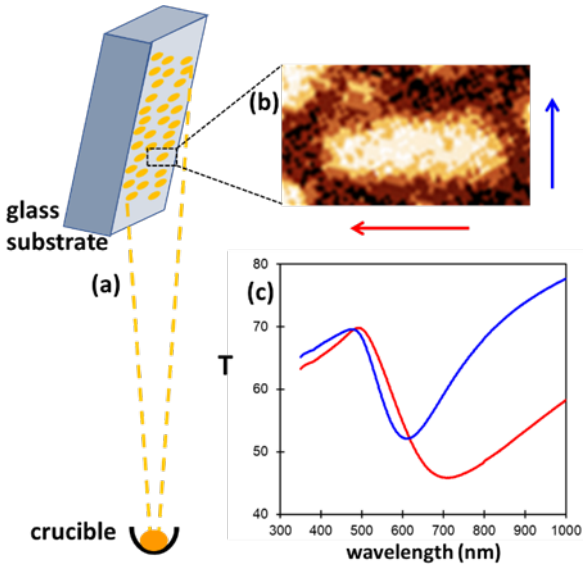

Scheme 1. (a): scheme of the grazing incidence deposition. (b): SEM image of an anisotropic NP. (c): transmission spectra T (%) as a function of the wavelength, for the two polarizations of light.

In the first part, we analyze the gold NPs' morphologies, which are on average elongated normal to the deposition direction, and whose shape is explained by the shadowing effect and correctly reproduced using a Monte-Carlo simulation of the growth at the atomic scale. Secondly, we show that the dichroism of these films is directly related to the anisotropic shape of the NPs. Their optical response is very well reproduced within the dipolar model, where the NPs are described by ellipsoids in electromagnetic interaction. Then, we experimentally demonstrate the high bulk sensitivity to refractive index (RI) change, with a factor of merit defined for intensity-based sensor (FoM*) reaching the outstanding value of 23 000. Finally, the surface sensitivity to biomecules is explored by theoretically determining the effect of the adsorption of the biotin/avidin couple. An extreme limit of detection (LoD) can be reached, down to about four discrete avidine molecules adsorbed on a sample area of 1 μm^2.

EXPERIMENTAL METHODS

Elaboration of the gold films.

The gold films (I) to (IV) were prepared by vacuum evaporation on microscope glass slides. The substrates were successively cleaned with acetone and isopropanol, followed by rinsing with deionized water, which was removed from the surface by flushing with dry nitrogen. The gold

(99.999% purity) was placed in a tungsten crucible within a dedicated evaporation chamber with a base pressure of 10^{-6} mbar. A grazing incidence of 12° was set; the amount of deposited gold was measured with a quartz microbalance located close to the samples, which was calibrated to account for the deposition angle. The glass slides were let at room temperature and were slightly heated by the crucible during the deposition, and their temperature reached about 310 K; the rate of deposition was kept at 0.024 +/- 0.004 nm/s during the whole time of evaporation. After the deposition, the samples were annealed in air at temperatures ranging from 120°C to 140°C for 10 min, in order to increase their subsequent stability with time. Such annealing barely modified the shape and the distribution of the NPs, and consequently their optical response were quite constant, as shown in Figure S.1 of the Supporting Information. Higher temperature and longer annealing time was not used, because such treatment decreased and eventually destroyed the morphological and optical anisotropy of the films (see Fig.S.4 for annealing up to 220 °C). Two kinds of samples were obtained, depending mainly on the amount of gold: island type films, where the gold NPs remains individual, and percolated films, where the gold elongated structures result from the percolation of the gold NPs, in good agreement with previous investigations for Au deposited at room temperature on glass substrate, at normal incidence [25].

Scanning Electron Microscopy

The morphology of the gold films was analyzed with a Scanning Electron Microscope (SEM) model Zeiss Supra 40. The high voltage was fixed at 3 to 6 kV, with a working distance of 4 to 5 mm and an aperture of 7 μm. As the samples were prone to charging, a copper tape was placed on the surface close to the region of interest.

Optical measurements.

The samples' optical transmission were investigated at room temperature in air by use of a commercial spectrophotometer (CARY 5000), with light polarized either along or normal to the deposition direction, by means of a Glan-Taylor polarizer.

The transmission anisotropy measurements, either spectral or at a fixed wavelength, were performed with a home-made Reflection / Transmission Anisotropy Spectrometer (RAS, TAS), based on Aspnes' configuration [18]. A detailed description of the set-up is given in the Supporting Information, part SI.2.

Refractive Index Sensitivity measurements

A commercial demountable cell from Perkin-Elmer was used for the measurements in liquid, using the sample as the entrance window. A mirror was placed after the cell, so that the optical beam passed a second time through the cell and the sample, transforming the RAS apparatus in a TAS apparatus. The liquid volume inside the cell was about 0.2 cm^2, and the exchange of liquid (e.g. from pure water to water/ethanol) was done by letting a volume of ca 5 cm^2 of the second liquid pass through the cell in 1 min, after which the liquid flux was stopped. During and after the exchange of solutions, some eddies perturbed the TAS measurements before the liquid stabilized, and the signal was not measurable for a few minutes.

The ethanol solutions with variable RI were made by diluting small amounts of ethanol (99.8% AnalaR Normapur) in ultrapure water (Millipore, 18.2 MΩ). Within the investigated RI range,

the increase of the RI is proportional to the concentration, varying from $n = 1.3330$ for pure water to $n = 1.3340$ for a volume concentration of ethanol of 2.11% (0.36 mol/L) [26].

The TAS of the samples installed in the cell were first measured in air, prior to filling the cell with water, after which the TAS was measured again. Filling and emptying several times the cell induced slight changes of the TA spectra, which was likely due to some modifications of the gold films. In order to avoid such modifications, the TA signal was monitored in pure water for a few tens of minutes, until it was stable. In the following, the samples were not exposed to air anymore, and the cell was successively filled by pure water or by alcohol solution. In order to avoid the formation of small bubbles in the cell (on the sample or on the windows), the liquids were deaerated by circulation of Ar for one hour before use. In spite of such procedure, it happened that some samples were not stable enough, when the cell was filled with ethanol/water mixing, in order to perform the RI sensing experiments, and they were eliminated. For future research and, in particular, for possible applications, it would be necessary to increase the stability of the gold NPs, for instance by functionalizing the glass substrate, and/or by protecting the gold deposit by a very thin inert dielectric, although this might decrease the NPs' sensitivity to their environment.

RESULTS AND DISCUSSION

Morphology of the Au nano-films elaborated at grazing incidence: microscopy results.

In the literature, Au anisotropic films have been obtained by deposition of the metal at oblique incidence onto nanostructured surfaces. Different substrates were used: faceted sapphire surfaces

obtained after high temperature annealing [27], alumina surfaces rippled by use of ion-beam sputtering [28], or homoepitaxially grown LiF [29]. These procedures indeed lead to the formation of chains of nanoparticles, inducing an optical anisotropy. However, the preparation of such substrates is quite involved and require specific treatments. On the other hand, it is known that depositing metal at grazing incidence on a smooth substrate without any specific preparation also yields different kinds of nanostructured films [30]. For thick layers, several hundreds of nms or more, the film is formed of rods obliquely erected on the surface. Whereas, for a small thickness typically less than 50 nm, the deposited film remains two-dimensional and the formed islands lie flat on the surface. Surprisingly, they are preferably elongated in the direction perpendicular to the direction of evaporation, as it has been observed previously, but relatively seldom exploited [31,32]. In this paper, this property is used in order to obtain anisotropic gold NPs films, through deposition at grazing incidence on ordinary glass slides, which display a strong dichroism, similar to the one obtained with the above-cited nanostructured substrates.

Growth of Au films by vacuum deposition close to the room temperature on glass slides has previously been thoroughly investigated [25]. It has been shown that the films are discontinuous and formed by Au NPs for mass thickness below ca. 7 to 10 nm, whereas they are percolated and formed by sinuous structures for larger thicknesses. The general morphology of the films depends on several parameters: the substrate temperature, the deposition rate, the total amount of gold, the possible post-annealing. The morphology is similar when deposition is performed at grazing incidence, with the important difference that they display morphological anisotropy, which consequently depends on the angle of deposition. Three typical samples (I), (II) and (III) are presented here, elaborated at a grazing angle of deposition of 12 +/- 1°, with Au mass thicknesses of 5.0, 9.4 and 22 nm, respectively, with a substrate temperature equal to 310 K and

rate of deposition equal to 0.024 ± 0.004 nm/s. Scanning Electron Microscopy (SEM) images of these samples are shown in Figure 1. Samples (I) and (II), with the smaller amounts of Au, are formed of separated NPs with a rather wide distribution of sizes, which, on average, are around 25 nm for (I) and 40 nm for (II). Generally speaking, the NPs display a slightly elongated shape and a smaller edge-to-edge distance in the direction normal to the deposition direction. The third sample (III), with a larger amount of Au, is different from the other two as percolation between the particles have occurred. It can be described by a set of long and sinuous structures, still in the direction perpendicular to the deposition, separated by narrow channels. The average anisotropy of the samples is also visible in the 2D Fourier transform patterns (Fig.1), which indeed display a slightly elongated shape rotated by 90° corresponding to the average shape of the NPs, with two internal lobes corresponding to the average distance between adjacent NPs. The homogeneity of the samples and the reproducibility of their elaboration, which are important issues for future applications, are discussed in the Supporting Information (Part SI.1), where large scale images of samples I to III and additional data for other samples are given. The effect of the deposition angle is also shown in Figure S.3, where two samples with close mass thicknesses (8.5 and 7.5 nm), elaborated at 32° and 12° respectively, are shown. We checked that in order to obtain subsequent anisotropy, an angle smaller than about 35° was needed. Finally, the effect of post-annealing is given in Figure S.4, showing that the optical anisotropy starts to reduce above 140°C, because of the mobility of the Au atoms.

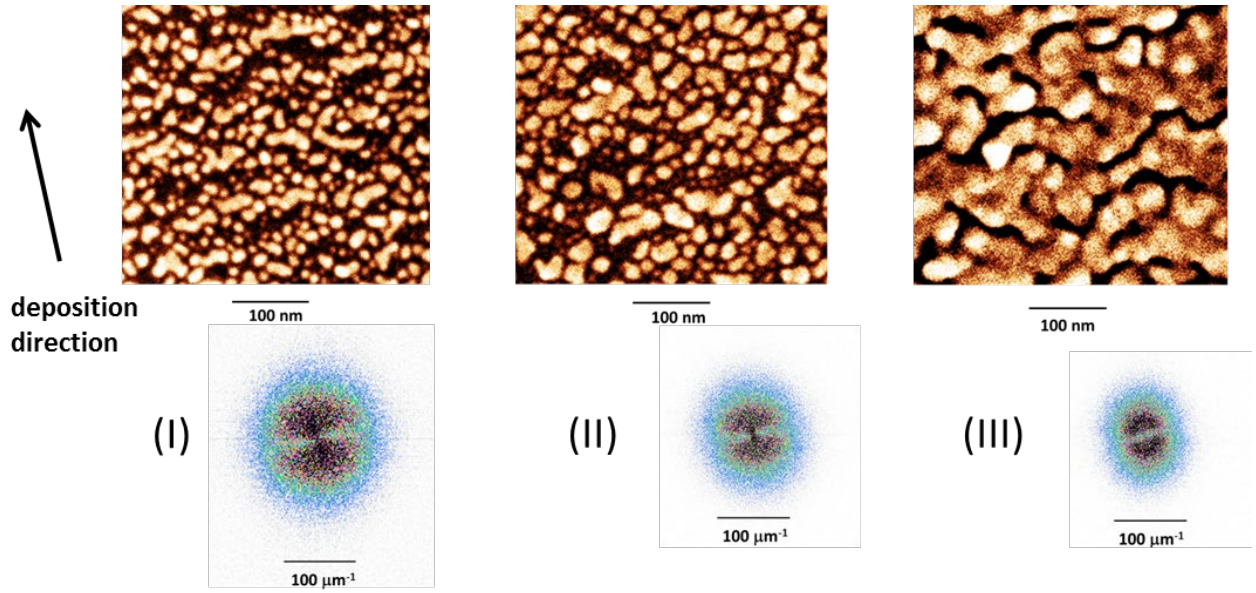

Figure 1. SEM images of three Au samples obtained with a 12° deposition angle, and their corresponding Fourier transforms. The mass thicknesses are 5.0, 9.4 and 22 nm, for films (I), (II) and (III), respectively.

The origin of the counterintuitive orientation of the elongated NPs, normal to the deposition direction, can be qualitatively explained by the self-shadowing effect [31], as illustrated in Figure 2: Au atoms diffuse on the glass substrate and form initial clusters (nucleation stage). The shadowing due to the grazing incidence creates an exclusion area behind the nucleus, where additional atoms cannot impinge, as schematized in Figure 2.a. The incident atoms diffuse and join the initial nuclei. Because of the exclusion areas, the lateral growth in the corresponding direction is reduced, thus yielding particles exhibiting anisotropic growth (dashed ellipses in Figure 2). This also leads to a bundling effect, that is a shorter distance between the particles in the direction normal to the deposition direction, as illustrated for a squared distribution of the NPs in Figure 2.c, which eventually leads to the coalescence of the NPs.

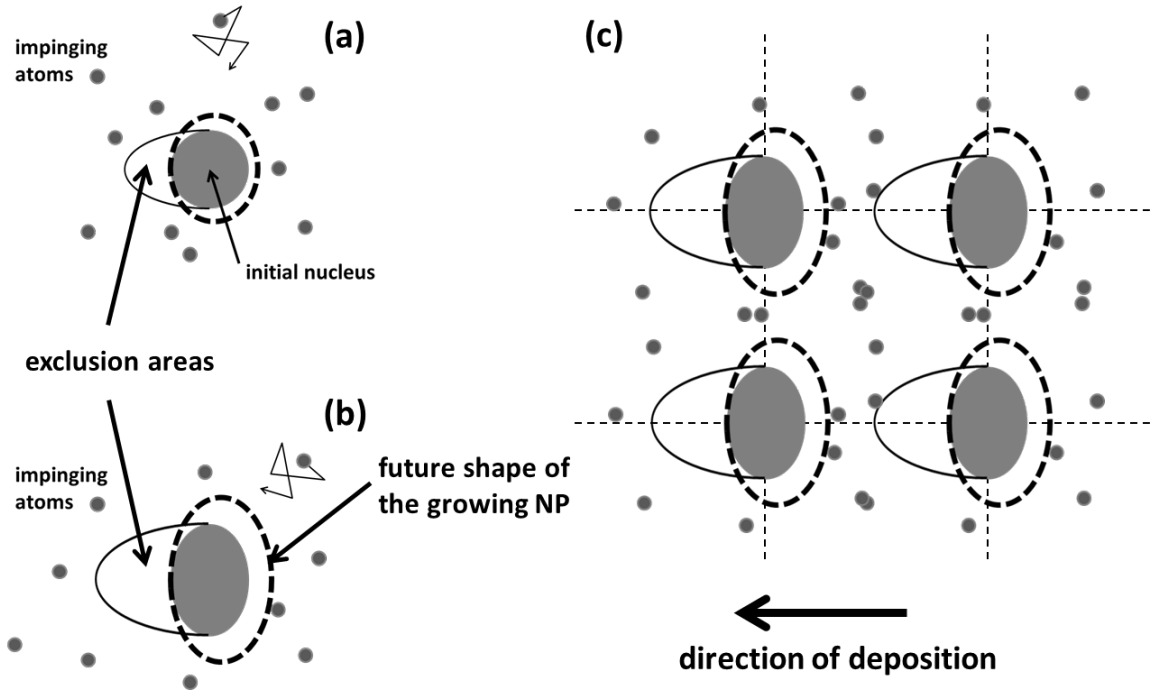

Figure 2. Diagram of the shadowing effect. (a) initial nucleus (grey disk), creating an exclusion area where atoms cannot impinge. The dashed ellipse indicates the growing of the nucleus after diffusion of the atoms arriving on the non-excluded areas. (b) similar shadowing effect for larger nanoparticles already exhibiting an anisotropic shape. (c) regular square distribution of the NPs showing shorter edge-to-edge gaps between NPs in the direction perpendicular to the direction of evaporation.

Morphology of the Au nano-films elaborated at grazing incidence: kinetic Monte Carlo modeling.

The experimental results are reproduced by use of a kinetic Monte Carlo (kMC) simulation of the growth at the atomic scale, that combines the ballistic sticking of impinging atom to the diffusion of already deposited atoms. The Au film is considered as a square array of elemental columns (*i,j*) with a lattice constant of 0.2569 nm, as shown in Figure 3.a. We employ the solid-on-solid model, where the occupation of a site in a column is allowed only if the site located below is already occupied [33]. Periodic boundary conditions are applied along the directions parallel to the surface. The kMC simulation is performed with the Bortz, Kalos and Lebowitz algorithm [34]. Briefly, each elementary process, including sticking or diffusion, is associated with a given frequency. At each kMC step, a random sampling is performed on all processes, accordingly to their respective frequencies. The time is increased by the inverse of the sum of all frequencies. Two classes of processes are considered. The first class is the sticking of an incoming atom, which frequency is given by the product of the flux and the area of the simulation box. In order to determine the site where this atom sticks, we proceed as follows: we consider an atom arriving from the right along direction *j* on the row i_0, with the grazing angle α (Figure.3.b). Three situations can occur: (1) it can impinge the glass substrate and stick on the arrival position (process A); (2) it can impinge and stick at the top of a column (process B); (3) it can impinge on the side of a column; in this case, in the solid-on-solid approach, it is considered that the atom, with equal probabilities, sticks either on top of the given column (process C) or at its base (process C*).

The second class concerns the diffusion of atoms already present on the film and located on top of the columns or on the substrate. Such atoms can perform single jumps to nearest neighbor columns, along the *i* and *j* directions and they are allowed to jump up or down a single or multiple steps (processes D and E of Figure.3.c). Each elemental move *k* is thermally activated

and associated with a frequency given by: $\nu_o \exp(-E_k/k_B T)$, where E_k is its activation energy and ν_o an attempt frequency. For a given diffusion or jump process k, the activation energy reads: $E_k = E_{diff,jump} + max(0, E_{final} - E_{initial})$, where $E_{diff,jump}$ is the diffusion or jump barrier energy, and E_{final} ($E_{initial}$) the final (initial) energy of the system. The energy of the system is obtained by a summation of pair interactions. The free parameters are the Au-glass bond energy ($E_{Au-glass}$), the Au-Au bond energy on the film (E_{b-gold}) or at the interface with the glass substrate ($E_{b-glass}$), the diffusion barriers for an isolated Au atom on the substrate ($E_{diff-glass}$), and for an isolated Au adatom on the film ($E_{diff-gold}$). An identical Ehrlich-Schwoebel barrier (E_{E-S}) has been also considered for jumps up or down a single or multiple steps. [35] All other diffusion barriers are derived from these parameters by adding a contribution proportional to the energy cost of the broken bonds during the diffusion, with a factor kept fixed to 0.3. ν_o has been kept fixed to 10^{12} s^{-1}. As all simulations are performed at the same temperature, it is clear that changing the value of ν_o has the same effect as changing the values of the diffusion barriers.

We have explored the space of free parameters in order to obtain simulated films corresponding with the SEM measurements. The images and the parameters corresponding to the best fit are given in Fig.4 and in Table 1. A detailed presentation of the evolution of the film morphology as a function of the parameters is presented in the Supporting Information, part SI.2.

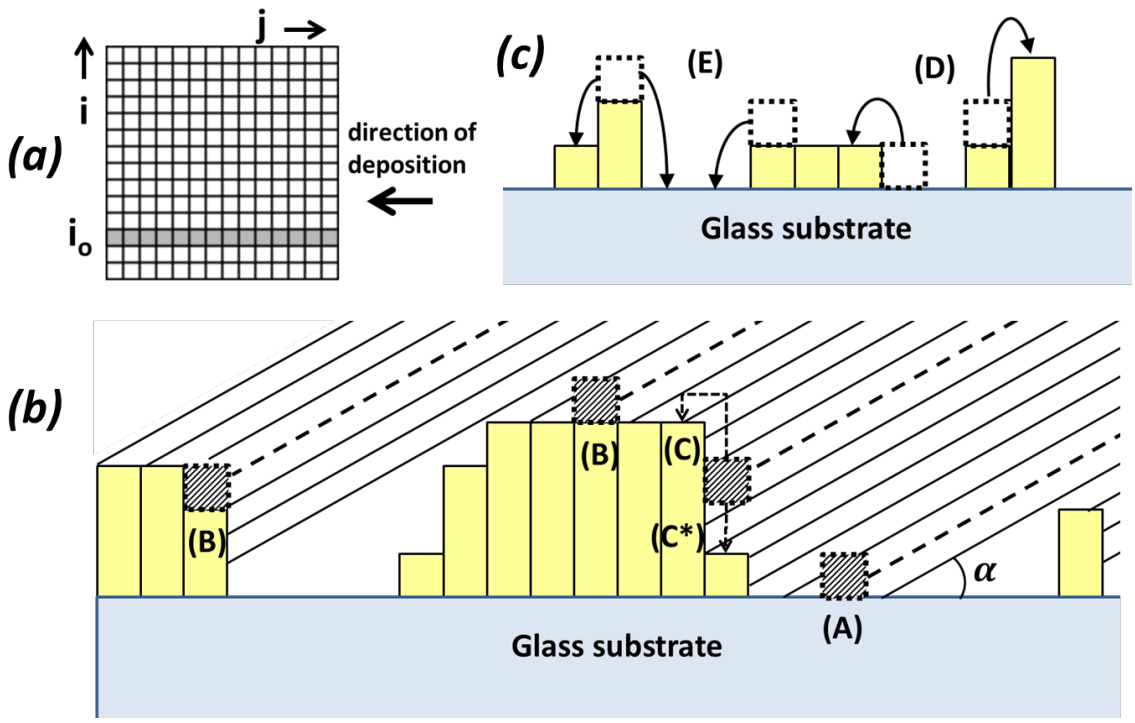

Figure 3. (a) Top view of the square array of gold columns on the substrate. (b) Diagram of the different adsorption processes along a row i_0 (side view): (A) adsorption on the substrate; (B) adsorption on top of a NP; (C) and (C*) impinging on the side of a column. The shadowing effect is also illustrated. (c) Jumping processes in play, step-up (D) and step-down (E).

The parameters used for optimizing the kMC results can be compared with data found in the literature. The diffusion barriers used in the kMC simulations that reproduced well the experimental results are in good agreement with values computed by DFT or semi-empirical potentials. [36–40] Indeed, the calculated energy barrier for Au self-diffusion on the (111) surface ranges between 0.015 eV and 0.25 eV, depending on the models and of the authors, and the corresponding attempt frequencies ν_o between 0.4 and 20.10^{12} s^{-1}. The energy barrier for self-diffusion on the (100) surface ranges between 0.26 eV and 0.64 eV, with attempt frequencies

between 7 to 50.10^{12} s^{-1}. To the authors' knowledge, no estimation has been given for the diffusion energy of Au atoms on glass. Even for well-defined oxide surfaces, information is sparse. Indeed the diffusion energies for Au on Al_2O_3, MgO and TiO_2 surfaces range between 0.16 and 0.28 eV [41–45]. Furthermore, it strongly depends of the presence of defects on the surfaces (oxygen vacancies, hydroxyl groups...).

It is more difficult to compare binding energies with experimental or computed ones since we have used a crude model where Au atoms are 6-fold coordinated. In the simulation, we have used an Au-Au bond energy, $E_{b-gold} = 0.59$ eV,which is very similar to the one derived from the experiments, assuming a pair summation of the bonds between nearest-neighbor atoms (i.e. $3.81 / 6 = 0.64$ eV). Concerning the bond energy between Au pairs at the glass interface, a slightly larger value is obtained, $E_{b-glass} = 0.70$ eV, which could reflects the fact that the bond between atoms is strengthened for smaller coordination number [46], for example at the surface or at the interface of a nanocrystal [47]. Finally, we remark that the value of the bonding energy between Au atoms and glass is small, $E_{Au-glass} = 0.078$ eV, as the experiments show that Au does not easily wet the glass substrate at room temperature and thus form compact islands.

The results for 310 K, the sample temperature during the deposition, are shown in Figure 4, for the two amounts of gold deposited at the angle of 12°, corresponding to samples (I) and (II). Due to the square symmetry used here, with diffusion allowed only in *x* and *y* directions, the simulated NPs display shapes close to the square equilibrium with the presence of right angles. This is of course not the equilibrium shape of an actual gold NP growing on a substrate without epitaxy relationship, which in fact would be truncated octahedron for Au particles of this size [48]. In spite of these differences due to the square lattice used, the results show a qualitative

agreement with the experiments, both for the size and for the elongated shape normal to the deposition direction. This indicates that the shadowing effect is indeed the driving force for the observed shapes. The NPs viewed with the SEM appear less structured and smoother than in the calculation, which is likely due to the fact that a hexagon is "rounder" than a square.

Table 1. Parameters used for the Monte Carlo calculations.

T	ν_o	$E_{diff-glass}$	$E_{diff-gold}$	E_{E-S}	$E_{b-glass}$	E_{b-gold}	$E_{Au-glass}$
310 K	10^{12} s^{-1}	0.23 eV	0.14 eV	0.03 eV	0.70 eV	0.59 eV	0.078 eV

T: temperature; ν_o: pre-factor diffusion; $E_{diff-glass}$: diffusion barrier of an isolated Au atom on glass; $E_{diff-gold}$: diffusion barrier of an isolated Au atom on gold; E_{ES}: Ehrlich Schwoebel barrier; $E_{b-glass}$: binding energy of a Au-Au bond for Au atoms located on glass; E_{b-gold}: binding energy of a Au-Au bond for Au atoms located on gold; $E_{Au-glass}$: binding energy of a Au-glass bond.

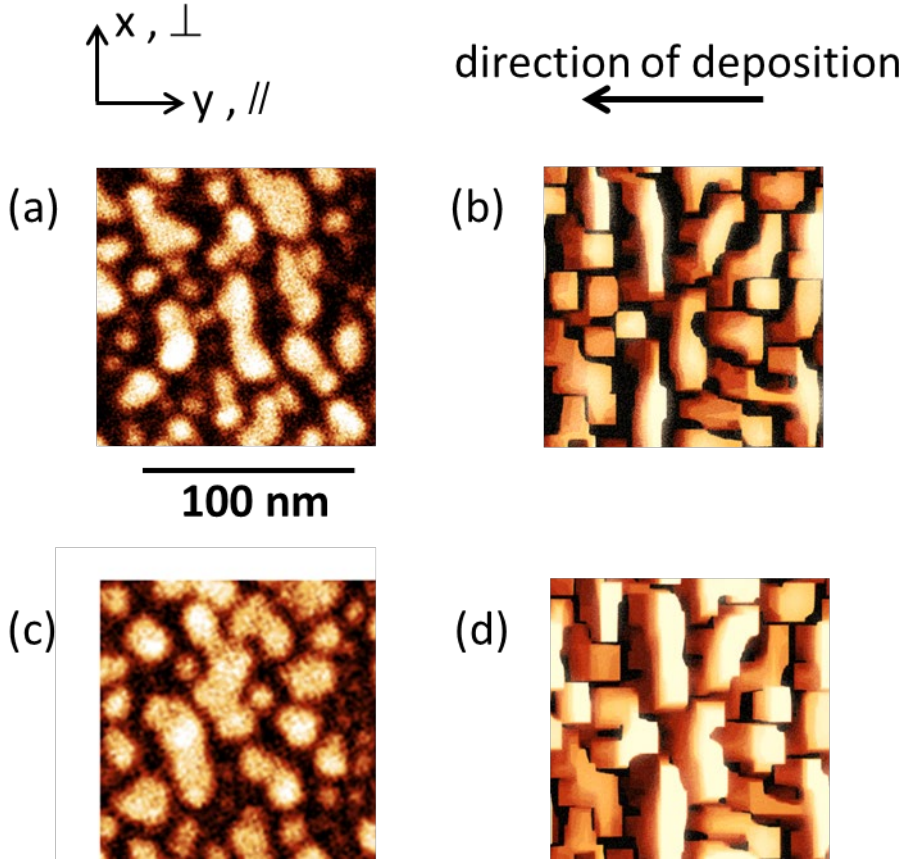

Figure 4. (a) and (c): zoom in of the SEM images of Figure 1 for samples (I) and (II), respectively; (b) and (d): Monte Carlo simulations for the same amounts of gold by using parameters given in Table 1. It must be noted that (b) and (d) are the simulation results with the same input parameters, but amounts of gold equal to 5.0 and 9.4 nm, respectively. Size: 132×132 nm^2. The direction of deposition is indicated by the arrow.

Dichroic transmission: experiment.

In this section the dichroic properties of the obtained anisotropic films are investigated. These optical properties are analytically modeled, enabling one to correlate the measured LSPR to the shape of the NPs. Transmission measurements in the ultraviolet - infrared range have been performed on the three selected samples, with light polarization parallel (//) and perpendicular (⊥) to the direction of deposition. The results are drawn in Figure 5 in dotted lines. For the two thinner films (I) and (II), the experimental transmission spectra are reaching the transmission of the glass substrate in the infrared (above about 1500 nm), meaning that the gold films are almost transparent in this wavelength range, which is characteristics of discontinuous gold films [49]. They also display clear minima in the visible range, due to the LSPR in the NPs. For sample I (resp. sample II), the LSPR is located at 580 nm (resp. 610 nm) in the // direction, which corresponds to the shorter axis of the NPs, and at a red-shifted wavelength of 680 nm (resp. 730 nm) in the ⊥ direction, corresponding to the longer axis of the NPs. This rather large dichroism (100 nm and 120 nm, respectively) is due, both to the anisotropic shape of the NPs, and to the bundling between them normal to the deposition direction. The third sample (III) shows a different behavior. The transmission is small in all the explored wavelength range, which is typical of a thin semi-transparent continuous (or almost continuous) layer, in agreement with the SEM picture. There is only a broad minimum around 700 nm, in the // direction, while no minimum is observed in the ⊥ direction. This can be interpreted as a plasmonic resonance located within the channels aligned in the ⊥ direction which separate the elongated islands.

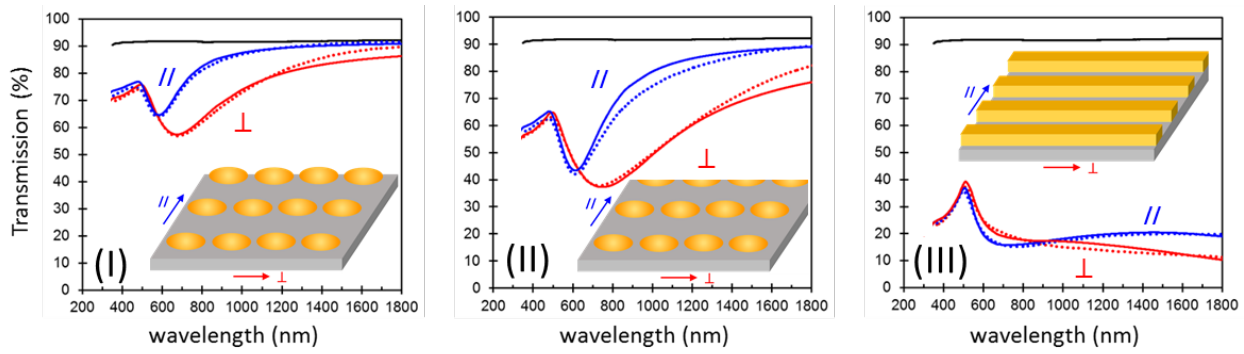

Figure 5. Transmission spectra of samples (I), (II) and (III), for polarization of light, parallel (blue) and perpendicular (red), to the direction of deposition. Dotted lines: experimental data; continuous lines: calculation based on the models schematized in the insets. The black curve is the transmittance of the bare glass slide.

Dichroic transmission: modeling

Rigorously modeling the optical response of discontinuous films formed by coupled islands of various shapes, such as those presented in Figure 1, is a difficult task, actually impossible with existing methods, even with a perfect knowledge of their morphology. Even for the simple case of an isolated particle deposited on a substrate, this is not trivial: if the particle is spheroidal, possibly truncated, with its axis of revolution perpendicular to the substrate, a multipolar approach is possible [50,51]. However, such a method is not usable for a different orientation of the spheroid, nor for ellipsoids without revolution axes, nor for a particle with arbitrary shape, like a realistic particle having facets and edges. In these cases, it would be possible to use finite element methods such as the Discrete Dipole Approximation (e.g. see Ref [52]), which can be used for isolated NPs [25]. However, it has been shown that, for a correct determination of the electric

field in the vicinity of the NPs and therefore of the LSPR coupling between the close NPs, the discretization has to be done with elements much smaller that $1nm^3$ [52]. The substrate also has to be discretized along a volume equivalent to that of the gold film, in order to account for the electric image effect. Such approach would then require one to consider a collection of several tens of NPs with their actual distribution of shapes, sizes and locations the ones with respect to the others, described by a number of discrete elements of several tens of millions that, in the present time, digital tools cannot grasp.

Alternatively, we use here the simpler dipolar approximation (DA), where every NP considered as a regular ellipsoid, is not discretized but described as a whole by a single point dipole, in electromagnetic coupling with the other NPs. All the point dipoles are taken as identical, which allows one to obtain an effective dielectric function describing the film. This model has been previously developed for ordered or disordered collections of NPs, in dipolar interaction with the substrate and with the other particles on the surface [53], and it allows one to reproduce the experimental observations very well, although it gives only an average description of the NP films. The assumptions we made here are the following: (a) the gold NPs are described by aligned ellipsoids located on a square array, their *y* axis being parallel to the deposition direction (as in Figure 2.c and in the insets of Figure.5.a and 5.b). (b) The NPs are treated within the DA, thus considered as point dipoles, with polarizability tensors $\alpha_{x,y}(\omega)$ given as:

$$\alpha_{x,y}(\omega) = 4\pi abc\frac{1}{3}\frac{\varepsilon_{Au}(\omega)-\varepsilon_{eff}(\omega)}{\varepsilon_{eff}(\omega)+L_{x,y}\left(\varepsilon_{Au}(\omega)-\varepsilon_{eff}(\omega)\right)} \qquad \text{(Eq. 1)}$$

where $\varepsilon_{Au}(\omega)$ is the dielectric function of Au [54], modified to account for the small NPs size [55] (see part SI.4 of the Supporting Information), $\varepsilon_{eff}(\omega)$ is the dielectric function of the effective medium in which the NPs are embedded, $L_{x,y}$ is the depolarization factor along x or y, and a, b

and c are the half-axis lengths of the ellipsoids along directions x, y and z [56]. The depolarization factors, ranging between 0 and 1, with $\sum L_j = 1$, determine the position of the LSPR obtained for the pole of Eq. 1: $\varepsilon_{Au}(\omega) = \varepsilon_{eff}(\omega)\left[1 - 1/L_j\right]$. The resonance is obtained for $\varepsilon_{Au}(\omega) = -2\varepsilon_{eff}(\omega)$ for a sphere ($L_j = 1/3$), and is shifted to smaller frequency, i.e. longer wavelength, for smaller values of L_j, in the long direction of the ellipsoid (see Table 2). (c) The interaction of the NPs with the substrate leads to a redshift of the plasmonic resonances. However, within the dipolar model where both the particle and its image particle are described by point dipoles, this interaction is overestimated, particularly for a flat particle [51]; consequently, the redshift due to this interaction is taken into account here by replacing the dielectric function of the ambient medium $\varepsilon_{med}(\omega)$ by an effective dielectric function, intermediate between that of the substrate and that of the ambient medium: $\varepsilon_{eff}(\omega) = 1/2\left[\varepsilon_{sub}(\omega) + \varepsilon_{med}(\omega)\right]$ [2]. (d) The interactions between the gold NPs are treated in the DA and are represented by an effective dielectric function [53]. (e) Multipolar resonances (beyond the DA) due to the interactions with the substrate [57] and between NPs [58] are not directly considered. These effects, in the case of gold NPs, essentially lead to a broadening of the resonances, which is accounted for phenomenologically and is added to the extrinsic broadening due to the distribution of particle shapes, as shown below.

Within this set of assumptions, the components of the dielectric function $\varepsilon_{film}(\omega)$ of the film of gold NPs along the two principal directions *x* and *y* in the plane of the layer read:

$$\varepsilon_{film}^{x,y}(\omega) = 1 + \frac{2f\frac{\alpha_{x,y}(\omega)}{4\pi abc}}{1-\frac{1}{2}\xi_o\frac{\alpha_{x,y}(\omega)}{4\pi abc}\left(\frac{f}{\pi}\right)^{3/2}} \qquad \text{(Eq. 2)}$$

where $f = \pi\, a\, b/D^2$ is the two-dimension filling factor. ξ_o is a geometrical constant equal to 9.03 for a square lattice of the NPs with parameter D [53]. Indeed, its value would be slightly different for instance in the case of triangle or rectangle lattices. In any case, regardless of the NP's distribution on the substrate, the denominator of Eq. 2 leads to a red shift of the LSPRs. Consequently, the use of a square lattice does not reduce the generality of our approach, and the obtained red shift could be simply adjusted by slightly changing the value of D in the calculation. It can also be noted that the calculation from Eq. 2 shows that the redshift for the perpendicular axis x is enhanced because of the closer gap between the NPs in this direction compared to the y direction, as it is illustrated in Figure. 2.c. Finally, because of the morphological distribution of the NPs, the gold NPs have LSPR slightly shifted with respect to each other, which leads to an extrinsic broadening of the plasmon resonances. To take this into account, the effective dielectric function (Eq. 2) is averaged on the basis of a Gaussian distribution around the mean values of the depolarization factors $L_{x,y}$ within Eq. 1.

The transmission spectra calculated for samples (I) and (II) for the two polarizations are drawn in continuous lines in Figure 5. The morphological parameters thus obtained, listed in Table 2, are in reasonable agreement with the SEM images of Figure 1. It should be noted that the agreement between the experimental and the calculated spectra is remarkable. This demonstrates that the use of this simple to apply analytical approach is indeed enough to describe the optical response of a complex assembly of NPs, even with a broad distribution of shape and size.

Table 2. Geometrical parameters obtained from the optical calculations, for samples (I), (II) and (IV), described as collections of coupled identical ellipsoids located on a square array, as shown in the insets of Fig.5 (I) and (II) and of Fig.6(a).

Sample	a (nm)	b (nm)	c (nm)	D (nm)	t_m (nm)	V (nm^3)	A (nm^2)	L_x $\lambda_{\perp}$ *(nm)*	L_y $\lambda_{//}$ *(nm)*	L_z	σ_x	σ_y
(I)	17.9	13.6	9.0	42.7	5.0	9177	2262	0.213 *680*	0.303 *580*	0.484	0.095	0.115
(II)	26.2	20.4	13.6	56.7	9.4	30448	5005	0.219 *730*	0.302 *610*	0.479	0.092	0.11
(IV)	30.6	19.8	12.6	64.8	7.62	31978	5394	0.176 *820*	0.310 *580*	0.514	0.110	0.115

a, *b* and *c*: average half-axis of the average NP along *x*, *y* and *z*, respectively [nm]; D: square lattice parameter [nm]; t_m: mass thickness of the films [nm]; V: volume of the average NP [nm^3]; A: surface area of the average NP [nm^2]; $L_{x,y}$: depolarization factor along *x* or *y* used as centers of the Gaussian functions [nm]; $\lambda_{\perp,//}$ corresponding resonance wavelengths in air [nm]; $\sigma_{x,y}$ standard deviations of the Gaussian functions.

On the other hand, the transmissions measured on sample (III), formed by very elongated islands separated by trenches, could not and should not be reproduced by this method. In place,

an alternative approach was used where the dielectric function of the film is given as the sum of the dielectric function of a continuous gold film and the effective dielectric function of gold stripes separated by empty trenches. This latter can be expressed as: [59]

$$\varepsilon^{x}_{stripe}(\omega) = g\ \varepsilon_{Au}(\omega) + (1-g)\ \varepsilon_{med} \qquad \text{Eq. 3.a}$$

$$\varepsilon^{y}_{stripe}(\omega)^{-1} = g\ [\varepsilon_{Au}(\omega)]^{-1} + (1-g)\ {\varepsilon_{med}}^{-1} \qquad \text{Eq. 3.b}$$

where *x* is parallel to the trenches and g is the lateral size of the stripes, $1-g$ being one of the trenches, normalized to 1, and $\varepsilon_{med} = 1$. A Gaussian averaging on g, around a mean value $g_{mean} = 0.94$ is in excellent agreement with the experiment as shown in Figure 5.III. The slight minimum around 700 nm for the // polarization indeed corresponds to a cavity plasmon-like resonance within the trenches of the films, while no resonance is obtained along the trenches (⊥ polarization), in agreement with the expression of Eq. 3.

Bulk sensitivity to refractive index change: enhanced FoM*.

A common method for determining the performance of plasmonic sensors is to check their bulk sensitivity to the change δn of the refractive index (RI), *n*, of the embedding medium. The bulk RI sensitivity (RIS) is defined as the ratio between the wavelength shift $\delta\lambda$ of the LSPR and δn: $\mathrm{RIS} = \delta\lambda/\delta n$, given in $\mathrm{nm.RIU^{-1}}$, where RIU is the refractive index unit [4]. The dimensionless factor of merit (FoM), given in $\mathrm{RIU^{-1}}$, characterizes the efficiency of a plasmonic sensor. Two FoM have been proposed, depending on the plasmonic sensing principle. For conventional plasmonic sensors, where the shift of the resonance wavelength is directly

measured, the FoM is defined by the ratio between the sensitivity RIS and the full width at half maximum FWHM of the resonance [4]: $\mathrm{FoM} = \mathrm{RIS}/\mathrm{FWHM}$. The sharper the resonance, the higher the accuracy for determining the shift. For plasmonic sensors based on the changes in intensity δI of the measured signal I at a fixed wavelength λ_o (e.g. reflection or transmission of light), an alternative FoM* has been defined as: [13,60]

$$\mathrm{FoM}^* = \frac{1}{I(\lambda_o)} \frac{\delta I(\lambda_o)}{\delta n} \qquad \text{Eq. 4}$$

An important challenge for LSPR sensing technologies is thus the improvement of the sensitivity *RIS*, the FoM or the FoM*, and eventually the limit of detection (LoD), which is the important and meaningful criterion for quantifying the actual sensitivity of a sensor [61]. Typically, for an ensemble of gold nanospheres in water, the RIS is equal to 90 nm.RIU^{-1} and the FoM to 1.5 RIU^{-1} (Ref [4]). Attempts to increase the RIS and FoM have been investigated by searching specific geometries for the Au NPs, like nanorods, bispheres, nanostars, nanocubes, bipyramids or nanomushrooms, [4,8–10,13] reaching values of RIS and FoM equal to 600 nm.RIU^{-1} and 5 RIU^{-1}. Decreasing the width of the resonance to increase the FoM has been further obtained by using Fano resonances, caused by the coupling between the NPs and other resonant nanostructures [9–12,62]. Enhanced FoM* have also been obtained for intensity-based sensing, by developing systems displaying a sharp fall of the transmissivity or the reflectivity, reaching almost zero at a given wavelength. This is the case with narrow-band "perfect absorbers", based on resonant nanostructured arrays, for which FoM* as large as 87 (Ref [60]), 104 (Ref [63]) and 900 RIU^{-1} (Ref [15,64]) were obtained.

This is the route we followed, based on the present anisotropic samples and the RAS apparatus, used in transmission mode, i.e. as transmission anisotropy spectroscopy (TAS). A

scheme of the set-up is shown in the Supporting Information, part SI.4. The TAS apparatus presented in this article allows one to directly measure, with high precision and stability, the normalized transmission anisotropy TA of the samples, defined by:

$$TA = \frac{\Delta T}{T} = \frac{T_{\perp} - T_{\parallel}}{1/2(T_{\perp} + T_{\parallel})} \quad \text{(Eq. 5)}$$

RAS apparatus has been initially designed in order to measure minute anisotropic signals of crystalline surfaces [19,24], and the sensitivity of RAS and of TAS can reach less than 10^{-5} (see part SI.5 of the Supporting Information). The system is mainly based on the combination of a phase modulator and a light polarizer [18]. In the present case the angle of the polarizer is adjusted in order to get a null value of the TA at a fixed wavelength, allowing to get a high accuracy and to measure very small changes.

For bulk sensitivity investigations, we now consider another sample (IV), whose transmission spectra are given in Fig.6(a). This graph shows that the sample is of NPs film type, and is similar to sample (II), although no SEM images where recorded. Its morphological parameters, determined from the optical transmissions, are given in Table 2. The sample was placed in the liquid cell, and the TA spectrum was directly measured, first when the cell was filled with air, then when filled with water. The measured TA spectra are drawn in Fig.6.b, and have a derivative-like shape: the positive and negative features are related to the LSPRs of the Au NPs in the parallel and perpendicular directions. The TA spectrum measured in water is nicely reproduced by the calculation with parameters given in Table 2, and is drawn with the thin blue line in Figure 6.b. It has to be noted that the polarizer has been rotated to get a null value of TA at $\lambda_o = 700$ nm for the sample in water. This wavelength corresponds to the largest slope $\delta I/\delta\lambda$ of the spectrum, which gives the highest sensitivity for sensing. The facts that the TA spectrum

has a derivative shape, and that we can chose a null signal at the wavelength of highest slope, by simply fixing the angle of the polarizer, are the key points which permit one to reach a highly enhanced sensitivity.

In a conventional plasmonic sensor, the detection of adsorbed entities on the plasmonic metal NPs is obtained by measuring the shift in wavelength of the LSPR, e.g. a redshift if the refractive index of the adsorbed layer is larger than the one of the solvent. In the present case of dichroic films with two different LSPR parallel and perpendicular, both resonances are also redshifted. It results in an overall redshift of the whole TA spectrum. This is illustrated in Figure 6.b, where the TAS is shifted by amounts varying from 30 nm at short wavelengths to 80 nm at long wavelengths, when the sample, initially in air with RI equal to $n = 1$, is introduced in water with RI equal to $n = 1.3330$. The redshift of the spectrum is not rigid, and is larger in the infrared, which explains why plasmonic sensors working in this range are generally more sensitive. Figure 6.c. is a zoom around $\lambda_o = 700\ nm$, where the TA has been adjusted to zero as explained above. The dotted red line is the spectrum measured for pure water, while the dashed red line is the measured spectrum for a mixing of water with 2.5% volume concentration of ethanol (0.43mol/L), with RI increased by $\delta n = 0.0014$ with respect to that of pure water. The redshift $\delta\lambda \approx 0.33$ nm of the TA spectrum due to this RI increase leads to an increase of the measured signal $I(\lambda_o) = TA(\lambda_o)$, at the given wavelength λ_o, by the value $\delta I(\lambda_o) \approx 0.001$, which is two orders of magnitude larger than the ultimate accuracy reached by TAS. This is the key issue of the method: rather than measuring the wavelength shift of the LSPR as in conventional plasmonic sensors, which is a difficult task for very small shifts, the change of the TA signal is measured at the single wavelength λ_o, where the TA signal has initially been fixed to the null value. Not only does it allow one to overcome the use of monochromator, it greatly

enhances the sensitivity of the system which is now mainly limited by the quality and stability of the electronic chain used in the detection apparatus.

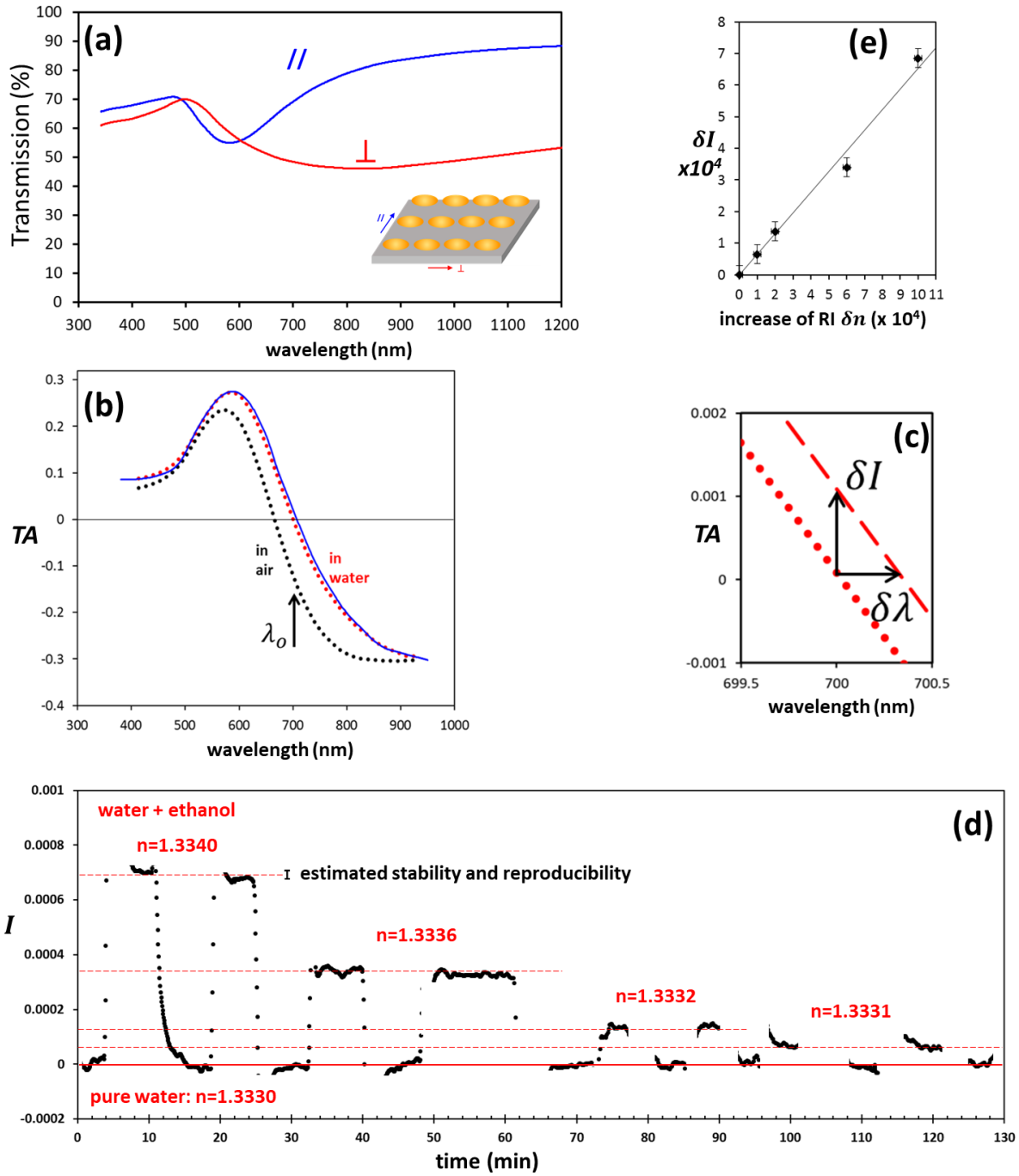

Figure 6. (a) Transmission spectra of sample (IV) measured in air, parallel and perpendicular to

the direction of deposition (mind the horizontal scale is different from the ones in Fig.5); (b) Transmission anisotropy spectra (TAS) of the gold sample (IV), measured in air (black dotted line) and in water (red dotted line). The thin blue line is the result of calculation using the parameters listed in Table 2. The arrow at 700 nm indicates the wavelength where the change of signal TA is monitored. Note that the TA spectrum has been shifted upwards by a chosen rotation of the polarizer (see Figure S.4 and S.7 of the Supporting Information), in order to get the null value in water at 700 nm, which explains that the crossing of the transmission curves in Fig.6.a does not correspond to the zero value in the TA measured in air. (c). Zoom of the TAS for the sample in pure water around 700 nm (dotted line) and in an ethanol solution at 2.5% (0.43 mol/L), with a small increase of the refractive index $\delta n = 0.0014$ (dashed line); the corresponding shifts of the wavelength $\delta\lambda$ and of the TA signal δI are shown by the arrows. (d) Signal I = TA at the wavelength of 700 nm, monitored during successive changes of the refractive index of the water/ethanol solutions, as a function of time. It took several minutes after exchanging the solutions in the cell before getting a stable signal: the signal displayed unstable variations during this transitory time and has not been drawn. (e) Variations δI of the signal TA as a function of the changes in the refractive δn index of the embedding liquid. Dots: experimental data; line: best linear fitting.

In the present case, as shown in Figure 6.c, the spectral shift at 700 nm when changing from water to water/ethanol mixing is 0.33 nm for $\delta n = 0.0014$. The value of RIS is therefore of the order of $235\,\mathrm{nm.RIU^{-1}}$. Considering the absolute value of the TA, the FWHM of this derivative-like resonance can be defined and is equal to 90 nm (see Fig.S.8 of the Supporting Information). If the system were used as a wavelength-shift based sensor, it would therefore lead to a conventional FoM of $235/90 = 2.6\ \mathrm{RIU^{-1}}$. These RIS and FoM values are indeed similar to what was obtained with nanoparticles of various shapes. In this current case, the system uses the intensity-based sensing mode and thus the alternative FoM* must be considered. As in the case of a perfect absorber, the measured quantity $I = TA$ reaches a null value at $\lambda_o = 700$ nm, and

the expression of the FoM* would lead to a theoretical infinite value. The value $I(\lambda_0)$ which has to be considered in the denominator of Eq. 4 is not, evidently, the null value, but the uncertainty δε of the measurement of the intensity $I = 0 \pm \delta\varepsilon$. This uncertainty corresponds to the stability and the reproducibility of the TA signal, which can be estimated equal to 2.5 10^{-5} in the present experimental conditions, as shown in Figure 6.d. The uncertainty on the position of the polarizer angle adjusted to get a null value is also to be considered. Accuracy around 0.1 arcsec is reached in the present experiment by use of a modified high-precision mechanical rotation stage from MKS Newport, leading to an additional uncertainty for the signal TA of about 0.5 10^{-5} (see Part SI.5 of the Supporting Information). This gives a total uncertainty in the present experiment $\delta\varepsilon \approx 3.\ 10^{-5}$. On the other hand, Figure 6.c shows that the ratio $\delta I/\delta n$ measured at $\lambda_o = 700$ nm in water is $0.001/0.0014 = 0.7\ \mathrm{RIU}^{-1}$. Consequently, the FoM* obtained in the experiment corresponding to Figure 6 reaches 23 000 RIU^{-1}. This value is about twenty-five times larger than previously experimentally obtained values for perfect Au- or Ag-based absorbers [15,64], and 20% larger than a theoretical result obtained for another Ag plasmonic perfect absorber [14]. This enhanced FoM* effectively corresponds to a very high RI sensing resolution, as it is demonstrated in the following.

In Figure 6.d, the variations δI of the signal $I = TA$ measured at 700 nm is monitored as a function of the changes in RI of the embedding medium filling the cell where the sample is placed. The measurements started with pure water ($n = 1.3330$) for which $I = 0$. Then, the pure water was alternatively replaced by an ethanol solution with decreasing RI from $n = 1.3340$ to $n = 1.3331$. Each solution was tested twice, in order to verify the reproducibility of the measurements. After flushing the solutions, it took a couple of minutes for the eddies to be suppressed, during which the TA signal was unstable and not recorded. The RI sensing

resolution reached in this experiment was better than $\delta n = 10^{-4}$. The variation of the signal δI as a function of the change δn is drawn in Figure 6.e. As expected for these small variations of δn, it follows a linear behavior. It can be noted that there is no intrinsic limitation to the obtained resolution. Better RI sensing resolution could indeed be obtained by increasing the integration time and by improving the counting electronic chain. The stability of the set-up and the reachable sensitivity is analyzed in part SI.5 of the Supporting Information, where it is shown that values of $\delta I < 10^{-5}$ can be reached. Moreover, some effort concerning the elaboration of the samples, in order to increase the sharpness of the slope of the TAS $\delta I/\delta\lambda$ at the working wavelength, should also allow one to increase the RI sensing resolution down to a few $\delta n \approx 10^{-5}$. Finally, it is worthwhile to note that, considering the nice simulation of the growth as demonstrated in Fig.4, it is feasible to modify the calculation parameters (flux, amount of gold, temperature, grazing angle) in order to predict the experimental conditions to obtain the most effective samples.

It is meaningful to compare the present results to other LSPR methods where the bulk sensitivity to small RI change δn have been measured. However, in most experiments, the changes of δn were higher than 0.01. After calculating the corresponding RIS, the authors usually extrapolate their results to smaller values of δn, on the basis of the estimated precision of the measured signal. It is surprising that very few LSPR-sensor experiments were actually performed for smaller values of δn, when such small changes are readily achieved and well controlled with alcohol solutions at varying concentrations. Several measurements for RI changes, δn, varying from 1.10^{-3} to 5.10^{-3} were published [10,15,16,63,65] though, to the authors' knowledge, only one group actually investigated smaller changes, by using "Au mushrooms arrays" prepared by a lithographic method, and demonstrated a sensing resolution of 2.10^{-4} (Ref [10]). The results presented in the present work are therefore at least two times more efficient than

this latter one. The remarkable point is that this demonstrates that the use of the present differential method, which is consequently a self-referenced method, working at a single wavelength, combined with the easily elaborated anisotropic gold samples, allows one to reach an excellent bulk RI resolution. This is equal or even better than what can be obtained with much more sophisticated LSPR samples prepared by electronic lithography, coupled with a high-resolution monochromator.

Theoretical surface sensitivity to biomolecular adsorption.

Although LSPR sensors can actually show a high bulk sensitivity to RI changes, as demonstrated in the previous section, they are not quite competitive with specific bulk RI sensing optical techniques based on propagating surface plasmons. Their interest mainly lies on their enhanced surface sensitivity to ions or molecules adsorbed at the surface of the NPs. This is related to the enhancement of the electromagnetic field associated to the LSPR in the immediate vicinity of the NP [4], making the LSPR very sensitive to the surface change of RI caused by the adsorbed entities, surface meaning in this context a distance smaller than the NP size. For an ellipsoid in a given medium with dielectric function $\varepsilon_{med}(\omega)$, the enhancement of the electric field of the LSPR at its surface, in the direction of the incident electric field, is given in the dipolar approximation by: [56]

$$\left|\frac{\varepsilon_{Au}(\omega)}{\varepsilon_{med}(\omega)+L\left(\varepsilon_{Au}(\omega)-\varepsilon_{med}(\omega)\right)}\right| \qquad \text{Eq. 6}$$

This gives, when using the modified dielectric function for Au (part SI.4 of the Supporting Information), the values of 6 for an isolated nanosphere in water, and of 23 for a nanoellipsoid with value $L_x = 0.176$ in the *x* direction, corresponding to sample (IV).

The shift of the LSPR wavelength caused by a shell of thickness d_s and refractive index n_s covering a NPs has been previously approximated by: [3]

$$\Delta\lambda = S\,(n_s - n_{med})\left[1 - exp\left(-\frac{2d_s}{l_d}\right)\right] \qquad \text{Eq. 7}$$

where n_{med} is the refractive index of the ambient medium ($\varepsilon_{med}(\omega) = {n_{med}}^2$) and l_d is the length of the EM-field decay associated to the LSPR, typically the radius for a sphere. Actually, we show in part SM.6 of the Supporting Information that a slightly better estimation of the shift is given by the formula:

$$\Delta\lambda = S\,(n_s - n_{med})\left[1 - \left(\frac{{l_d}^*}{{l_d}^* + d_s}\right)^3\right] \qquad \text{Eq. 8}$$

where l_d^* is also of the order of the radius. This is in agreement with the $1/r^3$ decrease law of the electric field for a dipole. These formulae clearly show the sensitivity of the NPs to a thin shell of adsorbed molecules. In the following, the sensitivity to molecular adsorption of the gold plasmonic sensor, investigated in the previous part, is calculated for the case of realistic biomolecules.

A common method for testing a biomolecule sensor is to investigate its sensitivity to the biotin/avidin couple, molecules known to display a very large affinity with each other. One usually considers the Au NPs to be covered by a layer of biotin, and test the change of the measured signal after adsorption of one or more avidin molecules. Biotin is a small biomolecule

of mass equal to 244 Da. Its size is approximately $1.2 \times 0.7 \times 0.6\,\mathrm{nm}^3$ with a volume of $0.24\,\mathrm{nm}^3$ [66]. A complete layer of biotin, lying flat and covering the surface, can be considered as a shell of about 0.6 nm average thickness, with a refractive index equal to 1.55, that of a dry protein layer [67,68]. Discussion is given in part SI.7 of the Supporting Information to show that the result is identical for a less dense layer with the same total number of proteins.

In the following calculations, the gold ellipsoids corresponding to sample (IV) are considered as core-shell ellipsoids described within the dipolar approximation [69]. The core is the same as the gold ellipsoids used in the spectrum of Figure 6.a. The 0.6 nm thick shell corresponds to the biomolecule layer. For the average NP surface area in sample (IV), equal to $\approx 5400\,\mathrm{nm}^2$, a complete biotin layer contains about 6000 molecules. As expected for such "thick" layer of molecules, the wavelength shift at 700 nm is rather large and equal to $6.5\,nm$, which is equivalent to a TA change of $\delta I = 0.019$, as it is shown in Figure S.11 of the Supporting Information. Such wavelength shift can of course be easily measured with a conventional LSPR sensor. Yet, the TA change is about 2 000 times larger than the ultimate sensitivity of the present system. As the effect of a few molecules bonded to a NP is similar to the effect of an additional layer around the NP with the same total volume (part SI.8 of the Supporting Information), this indicates that the adsorption of about three biotin molecule per NP could be measured.

The avidin is a large tetravalent molecule (67 kDa), with a molecular size of approximately $5.6 \times 5 \times 4\,\mathrm{nm}^3$ and a volume v_{av} which can be estimated to about 100 nm^3 (Ref [70]). Its size being smaller than the average size of the present NPs, its adsorption onto the NPs remains therefore in the "surface sensitivity" range of the system. The adsorption of one avidin molecule on the biotin-covered Au NPs is equivalent to a layer 0.018 nm thick (v_{av} divided by the area of

the average NP covered by biotin, equal to 5715 nm^2), leading to a change in the TA signal of 6.10^{-4}. With the optimal sensitivity of the apparatus equal to 10^{-5}, the limit of detection (LoD) that can be achieved would be 60 times higher, and would therefore correspond to one molecule adsorbed on a set of 60 NPs. With the average geometry of sample (IV) given in Table 2, this corresponds to a LoD of 4 molecules per μm^2 of the sample.

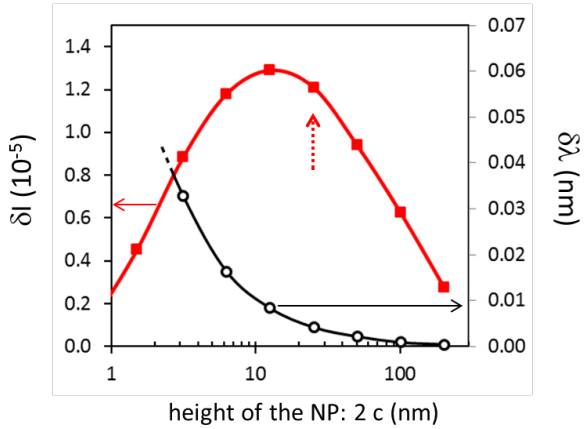

Figure.7. Red squares: calculated δI for an adsorption of 4 avidin molecules onto a set of Au ellipsoidal NPs covering a sample area of 1 μm^2 , as a function of the height of the average NP, i.e. the short dimension 2 c; black circles: corresponding wavelength shift. The dashed red arrow indicates the position of sample (IV).

At this stage, it is interesting to determine the optimal NP size that would be the most sensitive to such surface density of adsorbed molecules. One might think that it should be of the order of the molecule, or even less. This is the case if we are interested in the LSPR redshift: the smaller the NP, the more the adsorption of molecules on the surface will shift the resonance. However, with small NPs, i.e. small amount of gold covering glass, the LSPR would become very weak

and therefore its exact position and its shift would be difficult to measure correctly. Furthermore, the reduction of the conduction electron mean free path due to the reduced NP size dampens the resonance. Eventually the LSPR is nonexistent for Au clusters smaller than about 2 nm, which behave rather like large Au molecules than like metallic particles [71]. Using the modified Au dielectric function accounting for this size effect (part SI.4 in the Supporting Information), a realistic calculation is presented in Figure 7, for the expected wavelength shift $\delta\lambda$ of the perpendicular LSPR and for the change in signal intensity δI at 700 nm, as a function of the NP size (given by the quantity 2 c displayed in logarithmic scale). Four avidin molecule adsorbed on a sample area of 1 μm^2 was considered here, which is the estimated ultimate sensitivity of the present system. The wavelength shift remains below 0.01 nm for NPs larger than 10 nm, and increases only to 0.03 nm for a 2 nm high NP, which is the smaller size for which LSPR is defined in a Au NP. On the other hand, the values of δI are close to the maximum for NPs ranging between 4 nm to 80 nm. The dashed red arrow indicates the position of the average NP in sample (IV). This weak effect of the NP size is explained by the fact that, for large NPs the avidin has a relatively small effect on the LSPR shift, which is compensated by a large LSPR signal, whereas it is the opposite for smaller NPs, with larger LSPR shift but smaller LSPR signal. It is thus interesting to notice that the size of the NP is not crucial in order to get a very high sensitivity.

CONCLUSION

In summary, we experimentally demonstrated a high-sensitive self-referenced plasmonic sensor, by combining dichroic anisotropic gold films with measurement of their transmittance

anisotropy. The samples were obtained by simple vacuum deposition of gold on common microscope glass slides at grazing incidence. The gold formed elongated NPs lying on the substrate, displaying two different LSPR as a function of the polarization of the incident light. Their morphology was well reproduced by Monte Carlo calculation, and their optical response reproduced by calculations undertaken within the dipolar model. The transmittance anisotropy of the sample, which is intrinsically a self-referencing quantity, was fixed at the null value at the wavelength where its slope was the largest, which led to a strong enhancement of sensitivity of this plasmonic sensor. Due to the almost null value of the measured signal, the Factor of Merit, FoM*, defined for plasmon sensor based on intensity change, reached a value as large as 23 000 RIU^{-1}. Moreover, as measurements are performed at one fixed wavelength, no monochromator is needed, which strongly reduces the cost and the size of the system. The bulk sensitivity of this sensor was indeed demonstrated by experimentally determining a change of the refractive index of the ambient medium equal to $\delta n = 10^{-4}$. These experimental results allowed the theoretical demonstration of a high sensitivity to molecular adsorption, as four avidin molecules fixed onto on a sample area of 1 μm^2 could be determined with the present performances. A noteworthy conclusion was that this system does not require well defined nanoparticles. Furthermore, it was actually demonstrated that the optimum particle size is between 4 to 80nm, contrary to conventional wisdom where smaller NPs are usually better for these applications. This paves the way for the facile development of ultra-sensitive and low-cost label-free molecular sensors, reaching the single-molecule sensitivity. Furthermore, such system could be easily miniaturized, in order to be compatible with microfluidic systems or with lab-on-fiber technology[72].

ASSOCIATED CONTENT

Supporting Information Description.

The following file is available free of charge.

Additional SEM and optical data. Transmission Anisotropy Spectrometer set-up. Evolution of the film morphology: Monte Carlo results. Modification of the dielectric function of gold for taking account the small size of the NPs. Sensitivity and stability of the TAS apparatus; discussion of the FoM*. Determination of the FWMH of the TA spectrum. “Demonstration” of Eq.8. Effect of the density of the molecule layer. Comparison of the TAS for NPs without biotin and with a layer of 0.6 nm biotin covering all the NPs. Comparison of the optical response of a hetero-dimer Au NP / biomolecule and a core-shell (Au@biomolecule) NP.

AUTHOR INFORMATION

Corresponding Author

* Email: yves.borensztein@insp.jussieu.fr

Author Contributions

The manuscript was written through contributions of all authors. All authors have given approval to the final version of the manuscript.

REFERENCES

(1) Hutter, E.; Fendler, J. H. Exploitation of Localized Surface Plasmon Resonance. *Advanced Materials* **2004**, *16* (19), 1685–1706. https://doi.org/10.1002/adma.200400271.

(2) Kreibig, U.; Vollmer, M. *Optical Properties of Metal Clusters*; Springer, 1995.

(3) Anker, J. N.; Hall, W. P.; Lyandres, O.; Shah, N. C.; Zhao, J.; Van Duyne, R. P. Biosensing with Plasmonic Nanosensors. *Nature materials* **2008**, *7* (6), 442–453. https://doi.org/10.1038/nmat2162.

(4) Mayer, K. M.; Hafner, J. H. Localized Surface Plasmon Resonance Sensors. *Chemical Reviews* **2011**, *111* (6), 3828–3857. https://doi.org/10.1021/cr100313v.

(5) Halas, N. J.; Lal, S.; Chang, W.-S.; Link, S.; Nordlander, P. Plasmons in Strongly Coupled Metallic Nanostructures. *Chemical Reviews* **2011**, *111* (6), 3913–3961. https://doi.org/10.1021/cr200061k.

(6) Langer, J.; Novikov, S. M.; Liz-Marzán, L. M. Sensing Using Plasmonic Nanostructures and Nanoparticles. *Nanotechnology* **2015**, *26* (32), 322001. https://doi.org/10.1088/0957-4484/26/32/322001.

(7) Kedem, O.; Vaskevich, A.; Rubinstein, I. Critical Issues in Localized Plasmon Sensing. *J. Phys. Chem. C* **2014**, *118* (16), 8227–8244. https://doi.org/10.1021/jp409954s.

(8) Guo, L.; Jackman, J. A.; Yang, H.-H.; Chen, P.; Cho, N.-J.; Kim, D.-H. Strategies for Enhancing the Sensitivity of Plasmonic Nanosensors. *Nano Today* **2015**, *10* (2), 213–239. https://doi.org/10.1016/j.nantod.2015.02.007.

(9) Zhang, S.; Bao, K.; Halas, N. J.; Xu, H.; Nordlander, P. Substrate-Induced Fano Resonances of a Plasmonic Nanocube: A Route to Increased-Sensitivity Localized Surface Plasmon Resonance Sensors Revealed. *Nano Letters* **2011**, *11* (4), 1657–1663. https://doi.org/10.1021/nl200135r.

(10) Shen, Y.; Zhou, J.; Liu, T.; Tao, Y.; Jiang, R.; Liu, M.; Xiao, G.; Zhu, J.; Zhou, Z.-K.; Wang, X.; Jin, C.; Wang, J. Plasmonic Gold Mushroom Arrays with Refractive Index Sensing Figures of Merit Approaching the Theoretical Limit. *Nature Communications* **2013**, *4*, 2381. https://doi.org/10.1038/ncomms3381.

(11) Luk'yanchuk, B.; Zheludev, N. I.; Maier, S. A.; Halas, N. J.; Nordlander, P.; Giessen, H.; Chong, C. T. The Fano Resonance in Plasmonic Nanostructures and Metamaterials. *Nature Materials* **2010**, *9* (9), 707–715. https://doi.org/10.1038/nmat2810.

(12) Gerislioglu, B.; Dong, L.; Ahmadivand, A.; Hu, H.; Nordlander, P.; Halas, N. J. Monolithic Metal Dimer-on-Film Structure: New Plasmonic Properties Introduced by the Underlying Metal. *Nano Lett.* **2020**, *20* (3), 2087–2093. https://doi.org/10.1021/acs.nanolett.0c00075.

(13) Becker, J.; Trügler, A.; Jakab, A.; Hohenester, U.; Sönnichsen, C. The Optimal Aspect Ratio of Gold Nanorods for Plasmonic Bio-Sensing. *Plasmonics* **2010**, *5* (2), 161–167. https://doi.org/10.1007/s11468-010-9130-2.

(14) Yong, Z.; Zhang, S.; Gong, C.; He, S. Narrow Band Perfect Absorber for Maximum Localized Magnetic and Electric Field Enhancement and Sensing Applications. *Scientific Reports* **2016**, *6* (1), 24063. https://doi.org/10.1038/srep24063.

(15) Wang, Y.; Sun, C.; Li, H.; Gong, Q.; Chen, J. Self-Reference Plasmonic Sensors Based on Double Fano Resonances. *Nanoscale* **2017**, *9* (31), 11085–11092. https://doi.org/10.1039/C7NR04259K.

(16) Gao, B.; Wang, Y.; Zhang, T.; Xu, Y.; He, A.; Dai, L.; Zhang, J. Nanoscale Refractive Index Sensors with High Figures of Merit via Optical Slot Antennas. *ACS Nano* **2019**, *13* (8), 9131–9138. https://doi.org/10.1021/acsnano.9b03406.

(17) Chen, J.; Gan, F.; Wang, Y.; Li, G. Plasmonic Sensing and Modulation Based on Fano Resonances. *Advanced Optical Materials* **2018**, *6* (9), 1701152. https://doi.org/10.1002/adom.201701152.

(18) Aspnes, D. E.; Harbison, J. P.; Studna, A. A.; Florez, L. T. Reflectance-Difference Spectroscopy System for Real-Time Measurements of Crystal Growth. *Applied Physics Letters* **1988**, *52* (12), 957. https://doi.org/10.1063/1.99240.

(19) Weightman, P.; Martin, D. S.; Cole, R. J.; Farrell, T. Reflection Anisotropy Spectroscopy. *Reports on Progress in Physics* **2005**, *68* (6), 1251–1341. https://doi.org/10.1088/0034-4885/68/6/R01.

(20) Witkowski, N.; Coustel, R.; Pluchery, O.; Borensztein, Y. RAS: An Efficient Probe to Characterize Si(001)-(2×1) Surfaces. *Surface Science* **2006**, *600* (24), 5142–5149. https://doi.org/10.1016/j.susc.2006.08.045.

(21) Hogan, C.; Pulci, O.; Gori, P.; Bechstedt, F.; Martin, D. S.; Barritt, E. E.; Curcella, A.; Prevot, G.; Borensztein, Y. Optical Properties of Silicene, Si/Ag(111), and Si/Ag(110). *Physical Review B* **2018**, *97* (19), 195407. https://doi.org/10.1103/PhysRevB.97.195407.

(22) Verre, R.; Fleischer, K.; Sofin, R. G. S.; McAlinden, N.; McGilp, J. F.; Shvets, I. V. *In Situ* Characterization of One-Dimensional Plasmonic Ag Nanocluster Arrays. *Physical Review B* **2011**, *83* (12), 125432. https://doi.org/10.1103/PhysRevB.83.125432.

(23) Watkins, W. L.; Borensztein, Y. Mechanism of Hydrogen Adsorption on Gold Nanoparticles and Charge Transfer Probed by Anisotropic Surface Plasmon Resonance. *Phys. Chem. Chem. Phys.* **2017**, *19* (40), 27397–27405. https://doi.org/10.1039/C7CP04843B.

(24) Watkins, W. L.; Borensztein, Y. Ultrasensitive and Fast Single Wavelength Plasmonic Hydrogen Sensing with Anisotropic Nanostructured Pd Films. *Sensors and Actuators B: Chemical* **2018**, *273*, 527–535. https://doi.org/10.1016/j.snb.2018.06.013.

(25) Tesler, A. B.; Chuntonov, L.; Karakouz, T.; Bendikov, T. A.; Vaskevich, A.; Rubinstein, I. Tunable Localized Plasmon Transducers Prepared by Thermal Dewetting of Percolated Evaporated Gold Films. *J. Phys. Chem. C* **2011**, *115*, 24642–24652. https://doi.org/10.1021/jp209114j.

(26) *David R. Lide, Ed., CRC Handbook of Chemistry and Physics, Internet Version 2005, <http://Www.Hbcpnetbase.Com>, CRC Press, Boca Raton, FL, 2005.*

(27) Ualibek, O.; Verre, R.; Bulfin, B.; Usov, V.; Fleischer, K.; McGilp, J. F.; Shvets, I. V. Manipulating and Probing the Growth of Plasmonic Nanoparticle Arrays Using Light. *Nanoscale* **2013**, *5* (11), 4923–4930. https://doi.org/10.1039/C3NR00087G.

(28) Babonneau, D.; Camelio, S.; Simonot, L.; Pailloux, F.; Guérin, P.; Lamongie, B.; Lyon, O. Tunable Plasmonic Dichroism of Au Nanoparticles Self-Aligned on Rippled Al_2O_3

Thin Films. *EPL (Europhysics Letters)* **2011**, *93* (2), 26005. https://doi.org/10.1209/0295-5075/93/26005.

(29) Anghinolfi, L.; Moroni, R.; Mattera, L.; Canepa, M.; Bisio, F. Flexible Tuning of Shape and Arrangement of Au Nanoparticles in 2-Dimensional Self-Organized Arrays: Morphology and Plasmonic Response. *J. Phys. Chem. C* **2011**, *115* (29), 14036–14043. https://doi.org/10.1021/jp202230h.

(30) Barranco, A.; Borras, A.; Gonzalez-Elipe, A. R.; Palmero, A. Perspectives on Oblique Angle Deposition of Thin Films: From Fundamentals to Devices. *Progress in Materials Science* **2016**, *76*, 59–153. https://doi.org/10.1016/j.pmatsci.2015.06.003.

(31) Abelmann, L.; Lodder, C. Oblique Evaporation and Surface Diffusion. *Thin solid films* **1997**, *305* (1–2), 1–21. https://doi.org/10.1016/S0040-6090(97)00095-3.

(32) He, Y.; Fu, J.; Zhao, Y. Oblique Angle Deposition and Its Applications in Plasmonics. *Frontiers of Physics* **2014**, *9* (1), 47–59. https://doi.org/10.1007/s11467-013-0357-1.

(33) Zhdanov, V. P.; Rechendorff, K.; Hovgaard, M. B.; Besenbacher, F. Deposition at Glancing Angle, Surface Roughness, and Protein Adsorption: Monte Carlo Simulations. *J. Phys. Chem. B* **2008**, *112* (24), 7267–7272. https://doi.org/10.1021/jp709806k.

(34) Bortz, A. B.; Kalos, M. H.; Lebowitz, J. L. A New Algorithm for Monte Carlo Simulation of Ising Spin Systems. *Journal of Computational Physics* **1975**, *17*, 10–18. https://doi.org/10.1016/0021-9991(75)90060-1.

(35) Ala-Nissila, T.; Ferrando, R.; Ying, S. C. Collective and Single Particle Diffusion on Surfaces. *Advances in Physics* **2002**, *51* (3), 949–1078. https://doi.org/10.1080/00018730110107902.

(36) Boisvert, G.; Lewis, L. J. Self-Diffusion on Low-Index Metallic Surfaces: Ag and Au (100) and (111). *Phys. Rev. B* **1996**, *54* (4), 2880–2889. https://doi.org/10.1103/PhysRevB.54.2880.

(37) Davydov, S. Yu. Calculation of the Activation Energy for Surface Self-Diffusion of Transition-Metal Atoms. *Phys. Solid State* **1999**, *41* (1), 8–10. https://doi.org/10.1134/1.1130717.

(38) Chang, C. M.; Wei, C. M.; Chen, S. P. Self-Diffusion of Small Clusters on Fcc Metal (111) Surfaces. *Phys. Rev. Lett.* **2000**, *85* (5), 1044–1047. https://doi.org/10.1103/PhysRevLett.85.1044.

(39) Agrawal, P. M.; Rice, B. M.; Thompson, D. L. Predicting Trends in Rate Parameters for Self-Diffusion on FCC Metal Surfaces. *Surface Science* **2002**, *515* (1), 21–35. https://doi.org/10.1016/S0039-6028(02)01916-7.

(40) He, X.; Cheng, F.; Chen, Z.-X. The Lattice Kinetic Monte Carlo Simulation of Atomic Diffusion and Structural Transition for Gold. *Sci Rep* **2016**, *6* (1), 1–9. https://doi.org/10.1038/srep33128.

(41) Vitto, A. D.; Pacchioni, G.; Delbecq, F.; Sautet, P. Au Atoms and Dimers on the MgO(100) Surface: A DFT Study of Nucleation at Defects. *J. Phys. Chem. B* **2005**, *109*, 8040–8048. https://doi.org/10.1021/jp044143+.

(42) Barcaro, G.; Fortunelli, A. Structure and Diffusion of Small Ag and Au Clusters on the Regular MgO (100) Surface. *New J. Phys.* **2007**, *9* (2), 22–22. https://doi.org/10.1088/1367-2630/9/2/022.

(43) Chang, B. W.; Chou, J. P.; Luo, M. F. Adsorption and Diffusion of an Au Atom and Dimer on a θ-Al2O3 (001) Surface. *Surface Science* **2011**, *605* (11), 1122–1128. https://doi.org/10.1016/j.susc.2011.03.017.

(44) Jeon, J.; Yu, B. D. Adsorption and Surface Diffusion of Au Monomers and Dimers on Strongly Correlated NiO(001) Surfaces. *J. Phys. Soc. Jpn.* **2014**, *83* (11), 113602. https://doi.org/10.7566/JPSJ.83.113602.

(45) Iachella, M.; Le Bahers, T.; Loffreda, D. Diffusion Kinetics of Gold and Copper Atoms on Pristine and Reduced Rutile TiO_2 (110) Surfaces. *J. Phys. Chem. C* **2018**, *122* (7), 3824–3837. https://doi.org/10.1021/acs.jpcc.7b08183.

(46) Liu, X. J.; Zhou, Z. F.; Yang, L. W.; Li, J. W.; Xie, G. F.; Fu, S. Y.; Sun, C. Q. Correlation and Size Dependence of the Lattice Strain, Binding Energy, Elastic Modulus, and Thermal Stability for Au and Ag Nanostructures. *Journal of Applied Physics* **2011**, *109* (7), 074319. https://doi.org/10.1063/1.3569743.

(47) Huang, W. J.; Sun, R.; Tao, J.; Menard, L. D.; Nuzzo, R. G.; Zuo, J. M. Coordination-Dependent Surface Atomic Contraction in Nanocrystals Revealed by Coherent Diffraction. *Nature Materials* **2008**, *7* (4), 308–313. https://doi.org/10.1038/nmat2132.

(48) Barnard, A. S.; Lin, X. M.; Curtiss, L. A. Equilibrium Morphology of Face-Centered Cubic Gold Nanoparticles >3 Nm and the Shape Changes Induced by Temperature. *J. Phys. Chem. B* **2005**, *109* (51), 24465–24472. https://doi.org/10.1021/jp054279n.

(49) Norrman, S.; Andersson, T.; Granqvist, C. G.; Hunderi, O. Optical Properties of Discontinuous Gold Films. *Phys. Rev. B* **1978**, *18* (2), 674–695. https://doi.org/10.1103/PhysRevB.18.674.

(50) Bobbert, P. A.; Vlieger, J. The Polarizability of a Spheroidal Particle on a Substrate. *Physica A: Statistical Mechanics and its Applications* **1987**, *147* (1–2), 115–141. https://doi.org/10.1016/0378-4371(87)90101-4.

(51) Valamanesh, M.; Borensztein, Y.; Langlois, C.; Lacaze, E. Substrate Effect on the Plasmon Resonance of Supported Flat Silver Nanoparticles. *The Journal of Physical Chemistry C* **2011**, *115* (7), 2914–2922. https://doi.org/10.1021/jp1056495.

(52) Hao, E.; Schatz, G. C. Electromagnetic Fields around Silver Nanoparticles and Dimers. *J. Chem. Phys.* **2003**, *120* (1), 357–366. https://doi.org/10.1063/1.1629280.

(53) Barrera, R. G.; del Castillo-Mussot, M.; Monsivais, G.; Villaseor, P.; Mochán, W. L. Optical Properties of Two-Dimensional Disordered Systems on a Substrate. *Physical Review B* **1991**, *43* (17), 13819. https://doi.org/10.1103/PhysRevB.43.13819.

(54) Johnson, P. B.; Christy, R.-W. Optical Constants of the Noble Metals. *Physical review B* **1972**, *6* (12), 4370. https://doi.org/10.1103/PhysRevB.6.4370.

(55) Borensztein, Y.; Delannoy, L.; Djedidi, A.; Barrera, R. G.; Louis, C. Monitoring of the Plasmon Resonance of Gold Nanoparticles in Au/TiO_2 Catalyst under Oxidative and Reducing Atmospheres. *The Journal of Physical Chemistry C* **2010**, *114* (19), 9008–9021. https://doi.org/10.1021/jp101248h.

(56) Landau L.D.; Lifshitz E.M. *Electrodynamics of Continuous Media*; Pergamon Press, 1960.

(57) Beitia, C.; Borensztein, Y.; Lazzari, R.; Nieto, J.; Barrera, R. G. Substrate-Induced Multipolar Resonances in Supported Free-Electron Metal Spheres. *Physical Review B* **1999**, *60* (8), 6018. https://doi.org/10.1103/PhysRevB.60.6018.

(58) Bedeaux D; Vlieger J. *Optical Properties of Surfaces*, Imperial College Press.; London, 2001.

(59) Aspnes, D. E. Optical Properties of Thin Films. *Thin Solid Films* **1982**, *89* (3), 249–262. https://doi.org/10.1016/0040-6090(82)90590-9.

(60) Liu, N.; Mesch, M.; Weiss, T.; Hentschel, M.; Giessen, H. Infrared Perfect Absorber and Its Application As Plasmonic Sensor. *Nano Lett.* **2010**, *10* (7), 2342–2348. https://doi.org/10.1021/nl9041033.

(61) Unser, S.; Bruzas, I.; He, J.; Sagle, L. Localized Surface Plasmon Resonance Biosensing: Current Challenges and Approaches. *Sensors* **2015**, *15* (7), 15684–15716. https://doi.org/10.3390/s150715684.

(62) Zhan, Y.; Lei, D. Y.; Li, X.; Maier, S. A. Plasmonic Fano Resonances in Nanohole Quadrumers for Ultra-Sensitive Refractive Index Sensing. *Nanoscale* **2014**, *6* (9), 4705–4715. https://doi.org/10.1039/C3NR06024A.

(63) Lee, K.-L.; Chen, P.-W.; Wu, S.-H.; Huang, J.-B.; Yang, S.-Y.; Wei, P.-K. Enhancing Surface Plasmon Detection Using Template-Stripped Gold Nanoslit Arrays on Plastic Films. *ACS Nano* **2012**, *6* (4), 2931–2939. https://doi.org/10.1021/nn3001142.

(64) Zhou, J.; Liu, X.; Fu, G.; Liu, G.; Tang, P.; Yuan, W.; Zhan, X.; Liu, Z. High-Performance Plasmonic Oblique Sensors for the Detection of Ions. *Nanotechnology* **2020**, *31* (28), 285501. https://doi.org/10.1088/1361-6528/ab8329.

(65) Zeng, B.; Gao, Y.; Bartoli, F. J. Rapid and Highly Sensitive Detection Using Fano Resonances in Ultrathin Plasmonic Nanogratings. *Applied Physics Letters* **2014**, *105* (16), 161106. https://doi.org/10.1063/1.4899132.

(66) Pugliese, L. Crystal Structure of Apo-Avidin from Hen Egg-White. *J. Mol. Bio.* **1994**, *235*, 42–46.

(67) Liu, Z.; Qin, H.; Xiao, C.; Wen, C.; Wang, S.; Sui, S. Specific Binding of Avidin to Biotin Containing Lipid Lamella Surfaces Studied with Monolayers and Liposomes. *Eur Biophys J* **1995**, *24* (1), 31–38. https://doi.org/10.1007/BF00216828.

(68) Vörös, J. The Density and Refractive Index of Adsorbing Protein Layers. *Biophysical Journal* **2004**, *87* (1), 553–561. https://doi.org/10.1529/biophysj.103.030072.

(69) Bohren, C. F.; Huffman, D. R. *Absorption and Scattering of Light by Small Particles*; Wiley-VCH, 2004.

(70) Pugliese, L.; Coda, A.; Malcovati, M.; Bolognesi, M. Three-Dimensional Structure of the Tetragonal Crystal Form of Egg-White Avidin in Its Functional Complex with Biotin at 2·7 Å Resolution. *Journal of Molecular Biology* **1993**, *231* (3), 698–710. https://doi.org/10.1006/jmbi.1993.1321.

(71) Malola, S.; Lehtovaara, L.; Enkovaara, J.; Häkkinen, H. Birth of the Localized Surface Plasmon Resonance in Monolayer-Protected Gold Nanoclusters. *ACS Nano* **2013**, *7* (11), 10263–10270. https://doi.org/10.1021/nn4046634.

(72) Wang, Q.; Wang, L. Lab-on-Fiber: Plasmonic Nano-Arrays for Sensing. *Nanoscale* **2020**, *12* (14), 7485–7499. https://doi.org/10.1039/D0NR00040J.

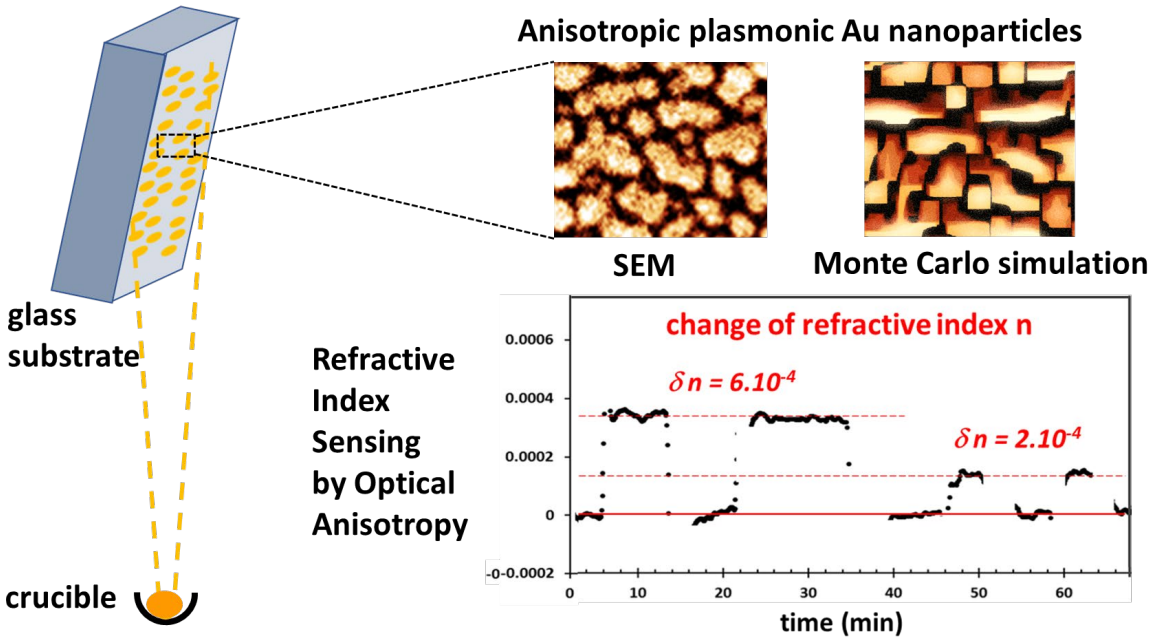

Table of Contents Graphics image